International Journal of Heat and Fluid Flow 50 (2014) 431–444

Contents lists available at ScienceDirect

International Journal of Heat and Fluid Flow

journal homepage: www.elsevier.com/locate/ijhff

Large-eddy simulation of the interaction of wall jets with external stream

Iftekhar Z. Naqavi [a],*, Paul G. Tucker [a], Yan Liu [b]

[a] Whittle Laboratory, Department of Engineering, Cambridge University, Cambridge, UK
[b] Department of Energy and Power Engineering, Dalian University of Technology, Dalian 116024, China

ARTICLE INFO

Article history:
Received 17 September 2012
Received in revised form 8 October 2014
Accepted 14 October 2014
Available online 8 November 2014

Keywords:
Wall jet
Turbulent boundary layer
Cutback trailing edge
Film cooling
Boundary layer wall jet interaction

ABSTRACT

Large eddy simulations are performed for a wall jet with an external stream. The external stream is in the form of a heated boundary layer. This is separated from a cold wall jet by a thin plate. The Reynolds number based on the displacement thickness, for the incoming boundary layer is 2776. A series of jet velocity ratios in the range $M = U_j/U_\infty = 0.30\text{–}2.30$, is considered. The wall jet and outer stream velocities are U_j and U_∞, respectively. The jets with $M \leqslant 1.0$ develop von-Karman type shed vortices in the wake region. The higher velocity ratio jets with $M > 1.0$ undergo Kelvin–Helmholtz instability and develop closely spaced counter-clockwise rolling structures. These structures determine the mean flow field behaviour and near wall heat transfer. At any given streamwise location adiabatic film-cooling effectiveness for $M < 1.0$ increases rapidly with increasing M. For $M > 1.0$ it decays slowly with further increase in M. For $M < 1.0$ heat transfer from the hot outer stream to the wall depends on two factors; mean wall normal velocity and wall normal turbulent heat flux. For $M > 1.0$ only a wall normal turbulent heat flux is responsible for heat transfer to the wall. The scaling behaviour shows that the near wall flow scales with wall parameters for all values of M. However, scaling in the outer region is highly dependent on M. The flow develops towards a boundary layer in the farfield for $M < 1.0$ and towards a wall jet for the highest velocity ratio $M = 2.30$.

1. Introduction

Plane, two dimensional wall jets have been studied extensively (Launder and Rodi, 1983; Schneider and Goldstein, 1994; Eriksson et al., 1998; Dejoan and Leschziner, 2005; Ahlman et al., 2007). Wall jets have a complex behaviour. The near wall region, called the inner layer, acts more like a turbulent boundary layer flow. The region away from the wall, or outer layer, acts like a free shear layer. They are also an idealised model for the outflow region of impinging jets and some meteorological phenomena (Lin and Savory, 2010).

In most practical situations wall jets usually have an external stream. Bradshaw and Gee (1962) and Verhoff (1963) made early fundamental studies on wall jets with external streams. They showed that for thin incoming boundary layers with no wake, the jet shear layer absorbs the boundary layer in a short distance. However, the presence of an external stream results in the involvement of several parameters. These include, the ratio of the wall jet bulk velocity, U_j, and the external stream velocity U_∞, i.e. $M = U_j/U_\infty$. Also, there are the thickness of the wake plate separating the two streams, incoming turbulence levels and the direction of incoming flows. These parameters determine the evolution of the wall jet. They can be controlled to produce the desired effects in wall jets, depending on their application.

The two major applications of wall jets with external streams are cutback trailing edge (TE) film cooling in gas turbines and the control of the boundary layers over high lift bodies, for example, Coanda jets (Nishino et al., 2010; Dunham, 1968). In both of these cases, wall jets interact with the external stream. However, the desired outcome of the interactions are completely opposite. In the case of TE film cooling a cold stream is introduced as a wall jet along the trailing edge. The objective is to keep the external hot stream (combustion gases) away from the wall, and, hence to avoid the mixing of the two streams as far downstream as possible. For the Coanda jet, to prevent the boundary layer separation a strong mixing of two streams is required. M is usually around 1.5 or less for TE film cooling and $M > 2.0$ for Coanda jet based flow control (Nishino et al., 2010).

In the case of TE film cooling, a major focus is the measurement and prediction of film-cooling effectiveness. Martini and Schulz (2004) performed measurements showing the importance of incoming turbulence. Recent large eddy simulations (LES) of TE

---

* Corresponding author.

http://dx.doi.org/10.1016/j.ijheatfluidflow.2014.10.014
0142-727X/

film cooling (Schneider et al., 2010; Schneider et al., 2012) for a series of blowing ratios M, in the range of 0.35–1.4, showed large coherent structures shed from the plate separating the two streams. With increasing M three different kinds of coherent structures appear. These are clockwise structures (CS), counter-clockwise structures (CCS) with CS and CCS only, for $M \leqslant 0.95, M \sim 1.25$ and $M = 1.40$, respectively. Moreover with increasing velocity ratios there are three distinct regions $[0.35; 0.65]$, $[0.65; 0.95]$ and $[0.95; 1.40]$, where the effectiveness of film cooling increased, decreased and then increased again. This unusual behaviour was associated with the strength and the rotation of the coherent structures present in the flow.

However, apart from jet velocity ratios the wake plate thickness has a strong influence on the film cooling effectiveness (Taslim et al., 1992). In previous studies (Schneider et al., 2010; Schneider et al., 2012) the wake plate thickness is of the order of the slot height. In the current work, extending the study of Taslim et al. (1992), a LES is performed on a simplified geometry. In the current work the wall jet and outer stream are parallel and separated by a thin wake plate around a tenth of the slot height.

Another important aspect, from the turbulence modelling perspective and a basic physical understanding, is the determination of self-similar behaviour of wall jets. Glauert (1956) has shown that complete self-similarity does not exist. Different velocity and length scales are required for inner and outer layers. Various parameters have been suggested to scale the mean velocity and Reynolds stress profiles. Narashima et al. (1973) suggested the jet momentum flux and kinematic viscosity as scaling parameters. These have been used to determine skin friction and show self similarity for a variety of jet nozzle Reynolds numbers (Wygnanski et al., 1992). George et al. (2000) have shown that with appropriate scaling, profiles collapse at infinitely large Reynolds number. For the inner layer, friction velocity u_τ and ν/u_τ are the velocity and length scales. The outer layer is scaled with maximum velocity U_{max} and $y_{1/2}$. The local maximum velocity in the wall jet at any given streamwise location is defined as U_{max}, where $y_{1/2}$ is the distance from the wall at which the velocity drops to half of its maximum value for a given streamwise location. The Reynolds shear stress in the outer layer scales with friction velocity u_τ^2, whereas normal stresses and mean velocities scale with maximum velocity U_{max}. In the presence of an external stream, a wall jet does not show self-similarity with the velocity and length scales noted above. Hence, in this paper we also present a scaling analysis to explore the similarity of the wall jet with an external stream.

2. Problem formulation

The interaction of wall jet with external stream is simulated with filtered conservation of mass and momentum equations for incompressible flow:

$$\frac{\partial \bar{u}_j}{\partial x_j} = 0 \tag{1}$$

$$\frac{\partial \bar{u}_i}{\partial t} + \frac{\partial \bar{u}_j \bar{u}_i}{\partial x_j} = \frac{1}{Re_{\delta_o^*}} \frac{\partial^2 \bar{u}_i}{\partial x_j \partial x_j} - \frac{\partial \bar{p}}{\partial x_i} - \frac{\partial \tau_{ij}}{\partial x_j}; \tag{2}$$

The $\bar{u}_i$ represents the filtered streamwise $\bar{u}$, wall-normal $\bar{v}$, and spanwise $\bar{w}$ velocity components respectively, in a Cartesian coordinate system. $\bar{p}$ is the filtered pressure. The Reynolds number is $Re_{\delta_o^*} = \frac{U_\infty \delta_o^*}{\nu}$, where δ_o^* is the displacement thickness of the inlet boundary layer and ν is the kinematic viscosity. The subgrid-scale (SGS) stresses, $\tau_{ij} = \overline{u_i u_j} - \bar{u}_i \bar{u}_j$, are modelled using the Lagrangian-averaged dynamic eddy-viscosity model (Meneveau et al., 1996).

To study heat transfer effects, a temperature transport equation is considered:

$$\frac{\partial \bar{T}}{\partial t} + \frac{\partial \bar{T} \bar{u}_i}{\partial x_i} = \frac{1}{Re_{\delta_o^*} Pr} \frac{\partial^2 \bar{T}}{\partial x_i \partial x_i} - \frac{\partial \bar{T}^{sgs}}{\partial x_i}; \tag{3}$$

where $\bar{T}$ is the filtered temperature, Pr is the Prandtl number and $\bar{T}^{sgs} = \overline{Tu_i} - \bar{T}\bar{u}_i$, is the sub-grid temperature flux. $\bar{T}^{sgs}$ is modelled following a dynamic eddy-diffusivity model (Moin et al., 1991).

These governing equations are discretised with a second-order collocated finite volume method, with a semi-implicit time advancement scheme. The convection term in Eq. (3) is discretized with the QUICK (Quadratic Upstream Interpolation for Convective Kinetics) scheme (Leonard, 1979). The Crank–Nicolson scheme is used for wall normal viscous terms and Adam–Bashforth scheme is applied to all other terms in the momentum equation. The solution of the Poisson equation is achieved by applying Fourier transforms in the spanwise direction and solving the resulting pentadiagonal system iteratively with a stabilised Bi-Conjugate gradient method. The code is parallelized with MPI and has been used in various LES studies previously (Radhakrishnan et al., 2006, 2008).

In this study, the focus is on the interaction of the wall jet with an external stream for a range of blowing ratios $M = 0.30$, 0.45, 0.60, 0.75, 0.90, 1.05, 1.20, 1.35, 1.50 and 2.3. The external stream is in the form of a fully developed turbulent boundary layer separated from the wall jet with a thin plate. This case has been studied experimentally by Kacker and Whitelaw (1971). At the inlet plane of the computational domain, the mean streamwise velocity profile for the wall jet exit and external boundary layer are available from the experiment. This data is used for the current simulations. The experimental boundary layer profile is used to determine δ_o^* and all lengths are normalised by this. The slot height of the wall jet is $h = 2.767\delta_o^*$ and the thickness of the plate separating the two streams is $t_w = 0.126h = 0.349\delta_o^*$. The inlet Reynolds number, based on the displacement thickness, is $Re_{\delta_o^*} = 2776$. Two different grids are used in this simulation and their details are summarised in Table 1. $L_x/h, L_y/h$ and L_z/h are the normalised streamwise, wall normal and spanwise domain dimensions, respectively. The fine grid is used for all the velocity ratios, the coarse grid is used only for $M = 0.75$ and 2.30 to allow a grid resolution study.

Fig. 1 shows a representative flow field in the domain. The mean profiles for the external stream and the wall jet at the inlet are available from the experiment and are shown in the Fig. 1, however, the time dependent turbulent information is missing. The experimental wall jet mean profile is slightly skewed and close to a channel flow profile. In order to add turbulent fluctuations a separate channel flow simulation is performed at a Reynolds number based on wall jet velocity and slot height. The instantaneous flow fields are saved for that simulation and mean streamwise velocity profile for the channel is removed from them. This results in fluctuating flow field u'. The level of turbulence at inlet is not known from Kacker and Whitelaw (1971). The fluctuations from the channel flow simulations are scaled and added into the mean experimental profile for the wall jet to provide a time dependent inlet boundary condition at the slot. Different values for that scaling factor are tested and a value of 0.2 is found suitable to reproduce experimental mean flow profiles, shown in the following section. Similarly, to generate turbulent fluctuations for outer stream a boundary layer simulation is performed with the recycling/rescaling method of Lund et al. (1998). The instantaneous flow fields are again saved for this case. Then again the mean boundary layer profile is removed and instantaneous fluctuations

Table 1
Summary of the domain and grid.

Grid	L_x/h	L_y/h	L_z/h	N_x	N_y	N_z
Coarse	80.0	16.0	5.5	512	145	64
Fine	45.0	16.0	5.5	1026	220	128

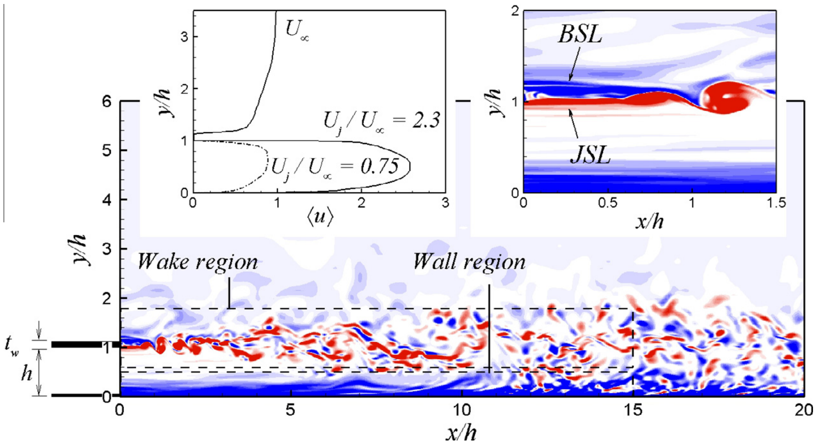

Fig. 1. Inlet velocity profiles from Kacker and Whitelaw (1971) and a typical instantaneous flow field represented by spanwise vorticity, with shear layer transition at $x = 1.0h$. Inset of shear layer closeup identify two shear layers separated by wake plate, i.e. jet side shear layer (JSL) and boundary layer side shear layer (BSL).

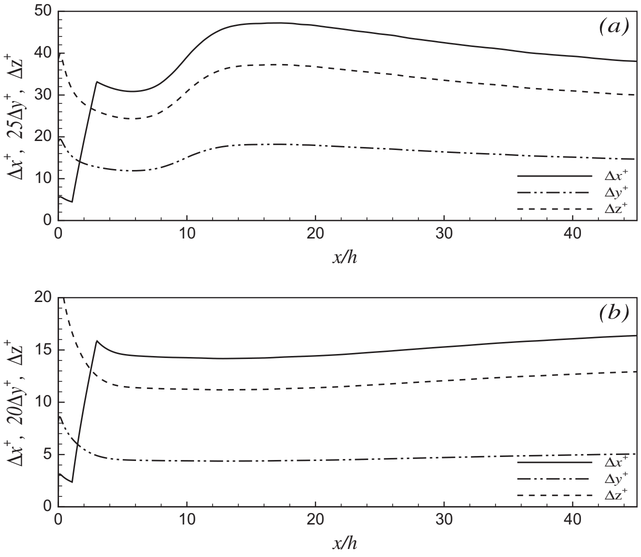

Fig. 2. Grid spacing variation along the streamwise direction in wall co-ordinates for the case of finer grid, (a) $M = 2.30$ and (b) $M = 0.75$.

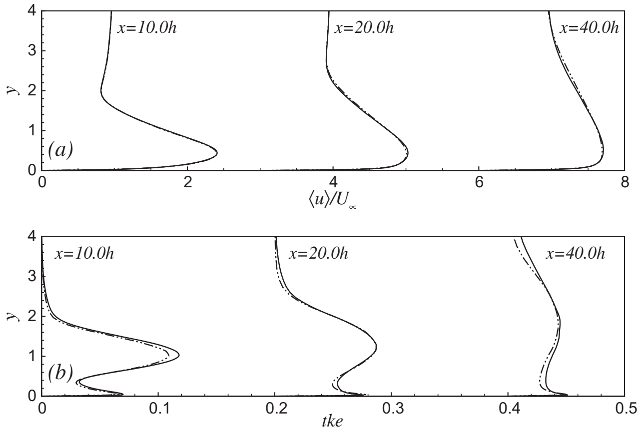

Fig. 3. Time averaged profiles of $M = 2.30$ jet at various locations for fine (—) and coarse (–··–) grids: (a) Mean streamwise velocity $\langle u\rangle/U_\infty$ and (b) turbulence kinetic energy $tke = 0.5 * (\langle u'u'\rangle + \langle v'v'\rangle + \langle w'w'\rangle)$.

are added to experimental profile without any scaling. These two time dependent velocity profiles with the zero velocity condition for the plate thickness, at the inlet plane, gives the inlet boundary condition for the domain. These inlet profiles are generated on coarser grids and interpolated on to the inlet plane of the main simulation. The incoming jet and boundary layer develop two shear layers, separated by the wake plate. These are designated here as the jet side shear layer (JSL) and the boundary layer side shear layer (BSL) (inset Fig. 1).

The other boundary conditions are specified as a no-slip boundary condition at the lower wall, and a free slip boundary condition at the top wall of the domain. At the exit plane, a convective boundary condition is applied (Orlanski, 1976). The spanwise direction has periodic boundaries.

For the temperature field, the incoming boundary layer flow has a uniform temperature of $T_h = 1.0$. The wall jet is at $T_c = 0.75$ and wake plate has a fixed temperature of 0.85. The lower and top walls of the domain are adiabatic. At the exit, a plane convective boundary condition is applied. The Prandtl number is $Pr = 0.71$.

3. Validation of simulation

The grid distribution is non-uniform in the streamwise and wall normal directions. The wall normal direction has a hyperbolic tangent stretching. Fig. 2 shows the fine grid distribution in the streamwise direction in wall co-ordinates for two jet velocity ratios. The high velocity ratio jet has a maximum $\Delta x^+ < 47.0$ and $\Delta z^+ < 38.0$. In wall normal directions, first off wall grid points are at $y^+ < 1.0$ with at least five points within the $y^+ = 5.0$ zone. The lower velocity ratio jet has maximum Δx^+ and $\Delta z^+ < 20.0$. The wall normal grid distribution has first grid points at $y^+ < 1.0$ and at least six points within $y^+ = 5.0$. The grid size normalised by h in the streamwise direction has $\Delta x = 0.01h - 0.06h$ with a stretching ratio less than 2%. The coarse grid for both velocity ratios jets has a Δx that is 60% larger and Δz twice that for the fine grid. In the wall normal direction the first grid points are again within $y^+ = 1.0$.

Fig. 3 shows mean streamwise velocity and turbulent kinetic energy (tke) profiles for the $M = 2.30$ jet at various locations for the coarse and fine grids. The grid effects are almost insignificant. The turbulent kinetic energy profiles have some differences, showing the effect of subgrid scales. However, the maximum difference in turbulent kinetic energy between the two grids is less than 8%.

The incoming turbulent boundary layer is validated through a comparison with the DNS data of Spalart (1988) and Schlatter et al. (2009) at $Re_{\delta_0^*} = 2000$. Fig. 4(a) shows that the mean velocity profiles $\langle u\rangle^+$ at the inlet is slightly shifted from the DNS data. However, the log-law behaviour is captured satisfactorily. Fig. 4(b) shows that the peak turbulence intensities are also in reasonable

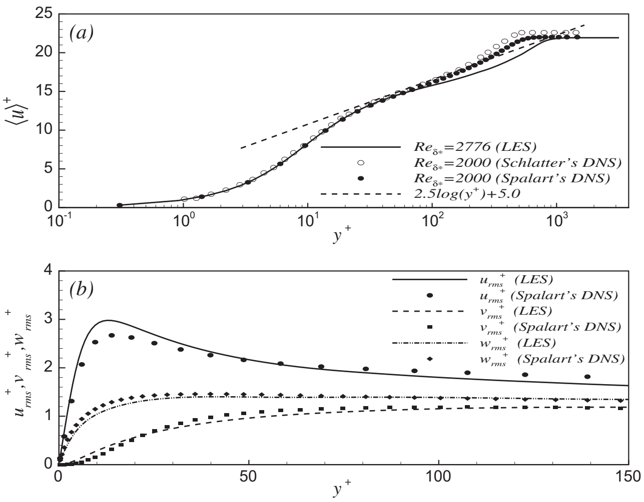

Fig. 4. Comparison of mean inlet profiles for incoming boundary layer with DNS data of Spalart (1988) and Schlatter et al. (2009) (a) mean streamwise velocity and (b) turbulent intensities.

agreement with the DNS data. The deviation of the inlet profile from the DNS away from the wall is due to the low resolution of the precursor boundary layer LES. There may also be insufficient dissipation from the sub-grid model (Porté-Agel et al., 2000). However, this will not have any significant effect on the current simulations. This is because the precursor LES is used to generate turbulence fluctuations, to be used along with the experimental mean profile at the inlet of the main simulation.

Fig. 5 compares the experimental data (Kacker and Whitelaw, 1971) at $x = 10h = 27.76\delta_o^*$ with the simulation. The solid lines are for the $M = 2.30$ and the dashes for the $M = 0.75$ jets simulation results, respectively. The symbols are the experimental data. The comparisons of the profiles for the mean flow and Reynolds stresses show that generally the strategy of specifying the profiles from the experiment and adding turbulence from separate simulations gives the same trends as in the experiments. The mean flow profiles, for both velocity ratio jets, are shown in Fig. 5(a) and (f) and are also in good agreement with the experimental data. The higher velocity ratio jet simulation gives better agreement for the Reynolds stresses $\langle v'v'\rangle/U_\infty^2$ and $\langle w'w'\rangle/U_\infty^2$ (Fig. 5(h) and (i)).

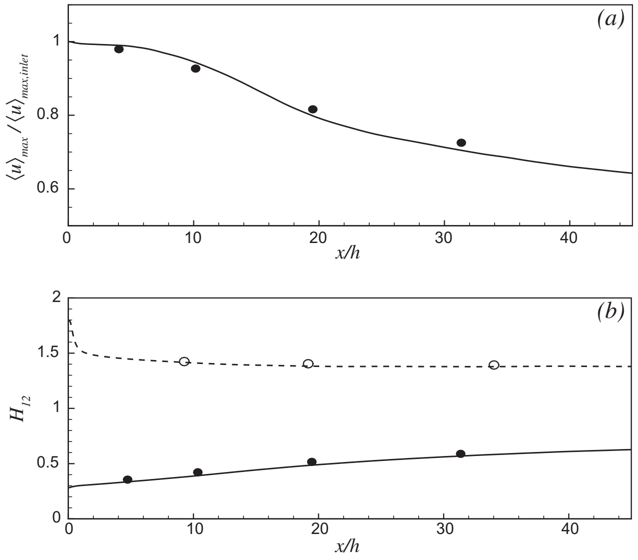

Fig. 6. Comparison of (a) velocity decay and (b) shape factor, from current simulation with the experiment (Kacker and Whitelaw, 1971). $M = 2.30$: — Current Simulation, • Experiment. $M = 0.75$: – – – Current Simulation, ○ Experiment.

However, the peak $\langle u'u'\rangle/U_\infty^2$ and $\langle u'v'\rangle/U_\infty^2$ (Fig. 5(g) and (j)) are much higher than the experimental value. This over-prediction may be the outcome of the uncertainty at the inlet in the simulation and in the hot-wire measurements. The Reynolds normal and shear stresses for the $M = 0.75$ jet are an order of magnitude smaller than for the $M = 2.30$ jet. The simulations over predict Reynolds stresses for $M = 0.75$. This may be due to the difference in the inlet turbulent fluctuations from the experiments. Fig. 6 shows that the velocity decay for the high velocity ratio jet and shape factor for both of the jets are in agreement with the experimental data.

4. Results

In this work our focus is to study the interaction of a wall jet with the outer boundary layer when the separation between the two streams, i.e. wake plate thickness t_w is relatively small. Previous studies, where a similar situation arises (Nishino et al., 2010;

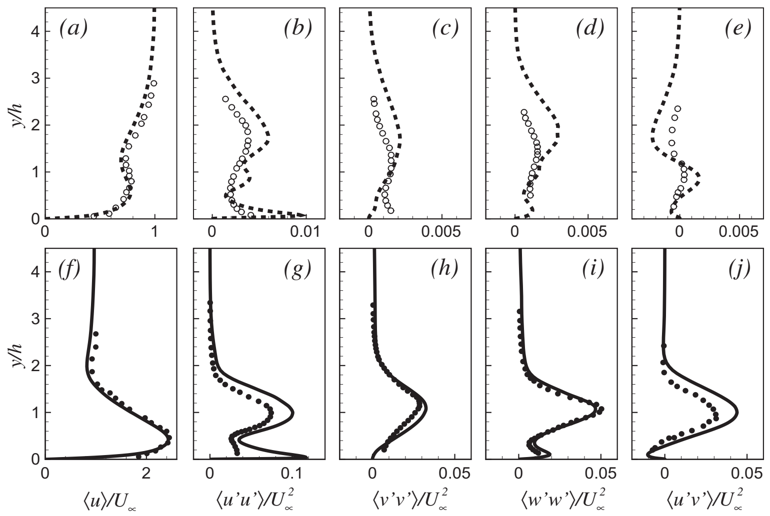

Fig. 5. Comparison of $\langle u\rangle/U_\infty$, $\langle u'u'\rangle/U_\infty^2$, $\langle v'v'\rangle/U_\infty^2$, $\langle w'w'\rangle/U_\infty^2$ and $\langle u'v'\rangle/U_\infty^2$ profiles at $x = 10h$ with the experimental data (Kacker and Whitelaw, 1971). (Top) $M = 0.75$: – – – Current Simulation, ○ Experiment. (Bottom) $M = 2.30$: — Current Simulation, • Experiment.

Schneider et al., 2010), have shown the existence of large scale coherent structures in the near wake region. These determine the mixing of momentum and heat between the wall jet and outer stream. The instantaneous flow field and mean quantities will be used here to show the development of structures and their effect on mean flow. All the results presented here are for the fine grid.

4.1. Development and dynamics of coherent structures

In the current simulation, various kind of vortical structures are involved. There are streamwise near wall structures from the incoming boundary layers and the slot jet. Apart from these structures, the interaction of the boundary layer with a wall jet generates further dynamic complexity, instability and more large scale structures. The coherent structures are visualised through isosurfaces of the second-invariant of the velocity gradient tensor $Q = -(\partial\langle u_i\rangle/\partial x_j)(\partial\langle u_j\rangle/\partial x_i)$ (Hunt et al., 1988; Dubief and Delcayre, 2000).

Fig. 7 shows the resulting coherent structures for jets with $M = 0.30, 0.60$ and 0.90. The structures for higher velocity ratio jets of $M = 1.05, 1.50$ and 2.30 are shown in Fig. 8. For clarity of the figures, the structures are shown only up to $x = 3.0h$. The right hand frames in each figure show the contours of the instantaneous spanwise vorticity $\omega_z = 0.5(\partial u/\partial y - \partial v/\partial x)$ in the wake region. The ω_z contours correspond to the three dimensional structures shown in the left frames and give their foot print at the $z/h = 0.0$ plane. The structures in the wake region are also coloured with spanwise vorticity. This makes it easier to identify the three dimensional structures and their footprint in the contour plots. The near wall structures coming from the wall jet are mainly in the streamwise direction and coloured with streamwise vorticity $\omega_x = 0.5(\partial w/\partial y - \partial v/\partial z)$. The negative ω_z vorticity for clockwise structures is coloured blue, whereas the positive vorticity for counter-clockwise structures is coloured red.

The structures in Fig. 7, for $M = 0.30$, give dominant clockwise structures (CS) on the BSL side. The JSL side vorticity is low. It does not form a really identifiable structure with the given Q iso surface criteria. With increasing jet velocity the JSL becomes stronger. For $M = 0.60$, the ω_z contours give alternate clockwise and counter-clockwise structures (CCS) in the wake region. The BSL clockwise

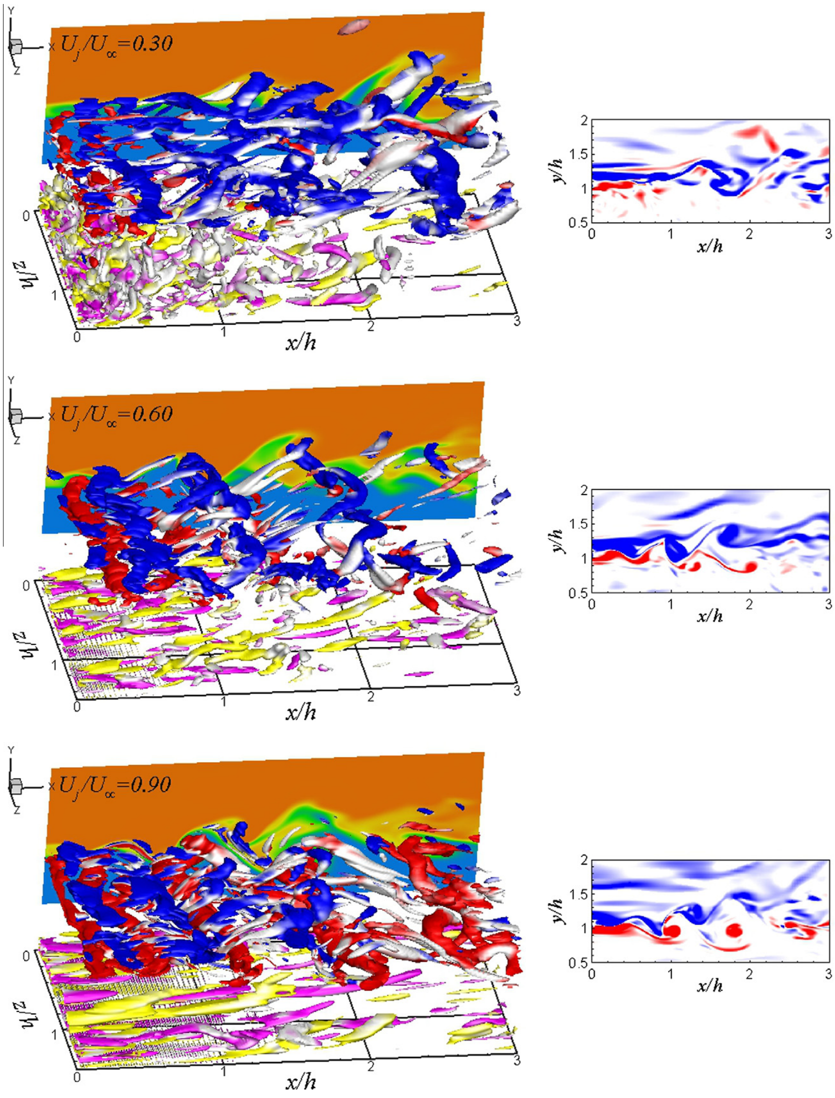

Fig. 7. Coherent structures in the near field region of wall jet and boundary layer interaction for low velocity ratio jets with $M = 0.30, 0.60$ and 0.90. (Left frames) Isosurfaces of $Q = 0.15$ away from wall and $Q = 0.06$ near the wall are used to visualise the structures. Isosurfaces are coloured with streamwise vorticity ω_x in near wall region and with spanwise vorticity ω_z in the wake region. Background $z/h = 0.0$ plane shows instantaneous temperature contours (with 20 equally spaced levels ranging over $T = 0.75$ to 1.0). (Right frames) Contours of spanwise vorticity at $z/h = 0.0$ corresponding to coherent structures in the wake region (with 20 equally spaced levels ranging over $\omega_z = -0.75$ to 1.25). (For interpretation of the references to colour in this figure legend, the reader is referred to the web version of this article.)

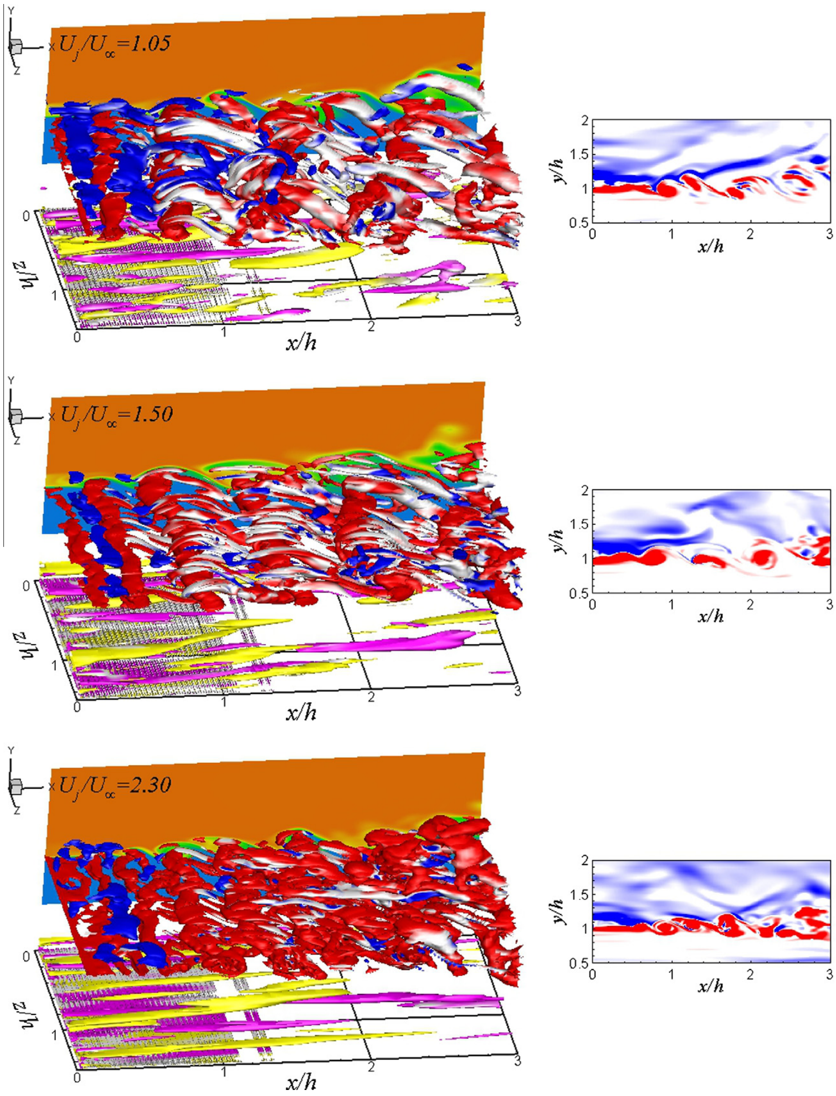

Fig. 8. Coherent structures for higher velocity ratios of $M = 1.05, 1.50$ and 2.30. (Left frames) Isosurfaces of $Q = 0.17$ away from wall and $Q = 0.075$ near the wall. Background $z/h = 0.0$ plane shows instantaneous temperature contours (with 20 equally spaced levels ranging over $T = 0.75$ to 1.0). (Right frames) Contours of spanwise vorticity at $z/h = 0.0$ (with 20 equally spaced levels ranging over $\omega_z = -0.85$ to 1.45). Colour scheme is same as in Fig. 7. (For interpretation of the references to colour in this figure legend, the reader is referred to the web version of this article.)

structures have higher vorticity magnitudes than the JSL counterclockwise structures. The BSL structures maintain their coherence up to $x = 2.0h$. The JSL structures are weak and lose coherence quickly. For $M = 0.90$, the JSL structures become stronger and maintain their coherence further downstream. The stronger JSL structures interact with BSL structures and diminish their coherence. The structures for $M < 1.0$ are like von-Karman shed vortices in a wake.

Fig. 8 shows that alternate CS and CCS disappear with increasing jet velocity ratio. The JSL, for $M = 1.50$ and 2.30, clearly undergoes Kelvin–Helmholtz (KH) instability and generates strong CCS. The average distance between the strong roll structures decreases with increasing jet velocity. There are streamwise structures stretched between the roll structures. The CCS, for $M = 2.30$, start to interact with each other just beyond $x = 1.0h$. The size of the structures, for both high and low velocity ratio jets, in the xy-plane is of the order of the wake plate thickness. The near wall structures are quite stretched in the streamwise direction, particularly for $M = 2.30$. They do not look like regular turbulent channel flow structures. This is because the incoming turbulent fluctuations are scaled with a factor of 0.2. This might result in the stretching of these weak structures by the fast moving outer flow.

4.2. Mean flow features and C_f

Fig. 9 shows a closeup view of time average streamwise velocity contours along with streamlines in the near wake region for various velocity ratio jets. The low velocity ratio jets, ($M < 1.0$), develop a mean counter rotating vortex pair in the recirculation region. This is to be expected for a flow in the wake of bluff bodies with shed von-Karman vortices. However, with increasing jet velocity the JSL side vortex diminishes in size. For higher velocity ratio jets with $M > 1.0$, there is only one mean vortex. This single vortex is formed when the boundary layer side fluid is dragged along with the jet side shear layer without forming any roll structure of its own. These streamline plots confirm that two different kinds of vortical structures develop in the near wake region.

In the current flow situation wall friction coefficient, $C_f = 2.0\tau_w/(\rho U^2)$, is defined with respect to the maximum local velocities U_{max} and U_∞. Fig. 10 shows the streamwise variation of C_f for various blowing ratios. The left frames in the figure give C_f for $M < 1.0$ and the right frames for $M > 1.0$. The C_f based on U_{max} and U_∞ for $M < 0.90$ collapse beyond $x = 30.0h$ (in this case U_{max}=U_∞, therefore Fig. 10(a) and (c) are identical). For higher

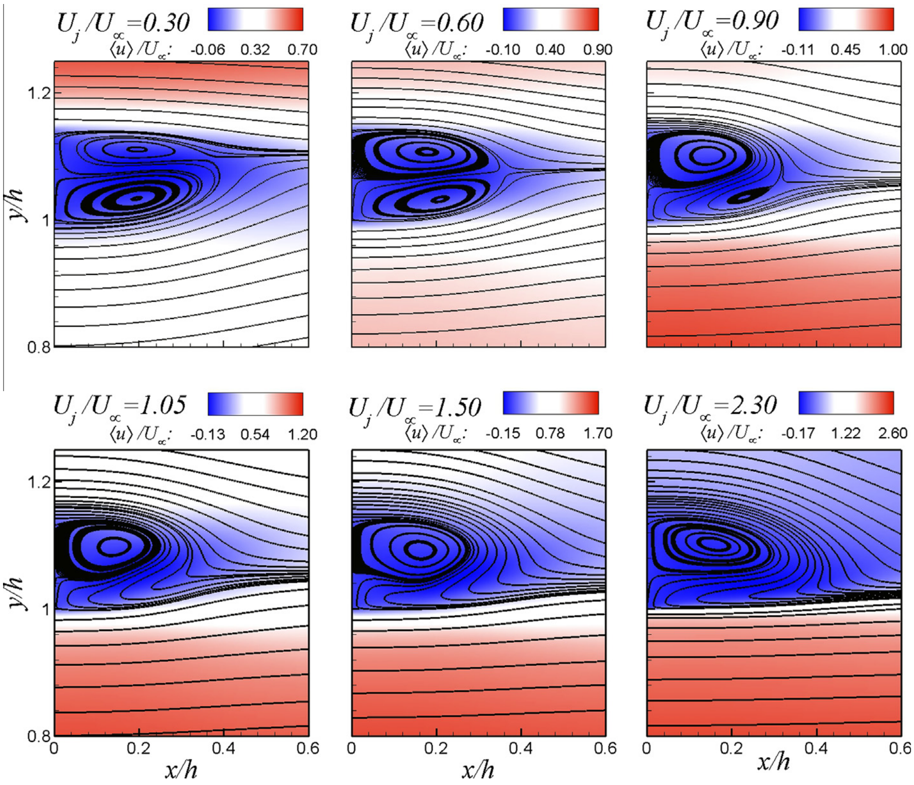

Fig. 9. Mean streamwise velocity contours and streamlines in the wake region near inlet plane for various velocity ratio jets.

velocity ratio jets with $M > 1.05, C_f = 2.0\tau_w/(\rho U_{max}^2)$ shows a collapse in the far-field. The $C_f = 2.0\tau_w/(\rho U_\infty^2)$ curves are compared with the experimental data (Kacker and Whitelaw, 1971) for $M = 0.75$ and 2.30. For $M = 2.30, C_f = 2.0\tau_w/(\rho U_{max}^2)$ is also compared with the experimental data (Kacker and Whitelaw, 1971).The simulated C_f values are lower than the experimental values, with a larger difference of 20% for higher velocity ratio jets. Following Patel (1965) there is a possibility that the Preston tube over-estimates wall friction for a wall jet with an external stream. However, simulations and experiment give identical trends for C_f. The variation of C_f along the streamwise direction is dependent on large scale wake structures. For low velocity ratio jets, e.g. $M = 0.75, C_f$ decays at a faster rate up to $x = 2.0h$. Beyond this location the near wall flow goes through transition under the influence of outer wake structures. This transition is slow and as a result, the C_f variation is gradual. For higher velocity ratio jets, for example, $M = 2.30, C_f$ decays rapidly near the inlet up to $x = 6.0h$. Beyond this location there is a sharp rise, which indicates a fast transition due to stronger wake vortices. The C_f plots show a non-monotonic variation with M, which is associated with a non-monotonic turbulence production in the outer shear layer region with increasing M. This is shown in the following sections. Fig. 10*(e)* shows the variation of C_f with local Reynolds number $Re_m = U_{max}y_m/\nu$, for $M > 1.0$, where y_m is the location of the maximum velocity U_{max}. With increasing M, both U_{max} and y_m increase at any given streamwise location. For comparison, the $C_f = 2.0\tau_w/(\rho U_{max}^2)$ values from an LES (Dejoan and Leschziner, 2005) and an experiment (Eriksson et al., 1998) of a plane wall jet are also included in Fig. 10. These values are higher than the current simulation. However, the trend is same, which suggests similar near wall behaviour for the two cases. It is important to mention here, that the C_f values for the plane wall jet from LES (Dejoan and Leschziner, 2005) are lower than the experimental values (Eriksson et al., 1998) at the same Reynolds number.

4.3. Mean velocity and Reynolds stresses

The development of the mean flow in the streamwise direction is shown in Fig. 11. The profiles are scaled with the local maximum velocity U_{max}. A wake is present in all mean streamwise velocity ($\langle u\rangle/U_{max}$) profiles (Fig. 11(a)). It is formed by the merging of the BSL and JSL. This is a direct consequence of the vortical structures present in the near field behind the wake plate. For $M > 1.0$ the velocity profiles also expand vertically, indicating spreading of the jets.

Mean wall normal velocity ($\langle v\rangle/U_{max}$) profiles (Fig. 11(b)) for $M = 0.30$ are negative. There is a sustained mean flow towards the wall. The profiles for $M = 0.60$ are positive in the near wall region at $x = 20.0h$. However, at farther downstream locations they also become negative. At higher velocity ratios ($M > 1.0$) the wall normal velocity remains positive up to quite large distances away from the wall. The wall normal velocity behaviour can be explained in terms of vortical structures formed in the wake region. For $M = 0.30$ strong CS form in the near field. They breakdown quickly but establish the dominant direction of rotation for smaller scale structures in the wake region. The wake entrains the external stream with these structures and develops a sustained flow towards the wall. The strength of CS decreases for $M = 0.60$ and as a result of this the mean wall normal velocity also decays. For $M > 1.0$ CCS mix high velocity jet fluid with the slow moving external stream. As a result the jet expands and decelerate. This gives a positive wall normal velocity. With increasing jet velocity ratios the CCS strength and subsequent mixing with the outer stream increases. This results in a larger jet expansion and higher positive wall normal velocity.

Fig. 12 shows streamwise development of normal and shear Reynolds stresses for various M. The profiles are scaled with U_{max}^2. The streamwise Reynolds stress ($\langle u'u'\rangle/U_{max}^2$) profiles show that in the far-field wake region, $M = 2.30$ has the highest values

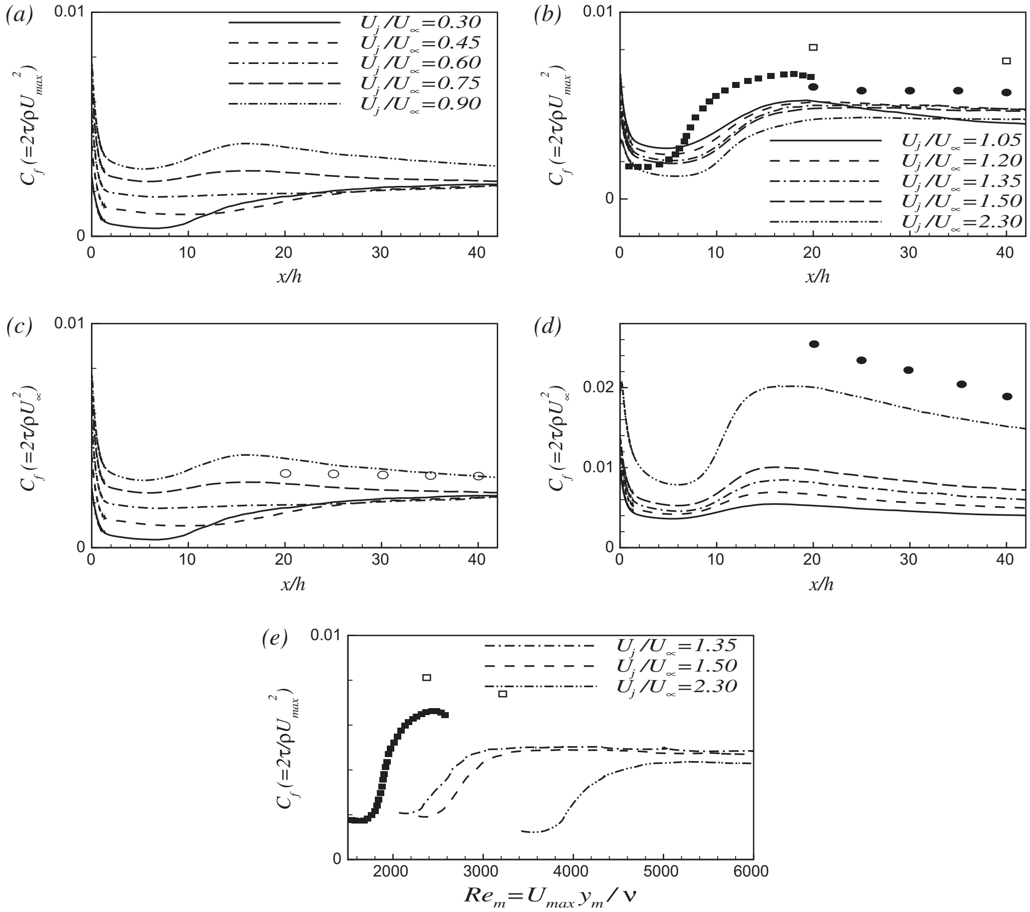

Fig. 10. Variation of wall friction coefficient along the streamwise direction. Left frames are for $M < 1.0$ and right frames are $M > 1.0$. (a) and (b) $C_f = 2.0\tau_w/(\rho U_{max}^2)$ and (c) and (d) $C_f = 2.0\tau_w/(\rho U_\infty^2)$. (e) $C_f = 2.0\tau_w/(\rho U_{max}^2)$ as a function of $Re_m = U_{max}y_m/\nu$. $M = 0.75$ (○) and $M = 2.30$ (●) Kacker and Whitelaw (1971), (■) Dejoan and Leschziner (2005), and (□) Eriksson et al. (1998).

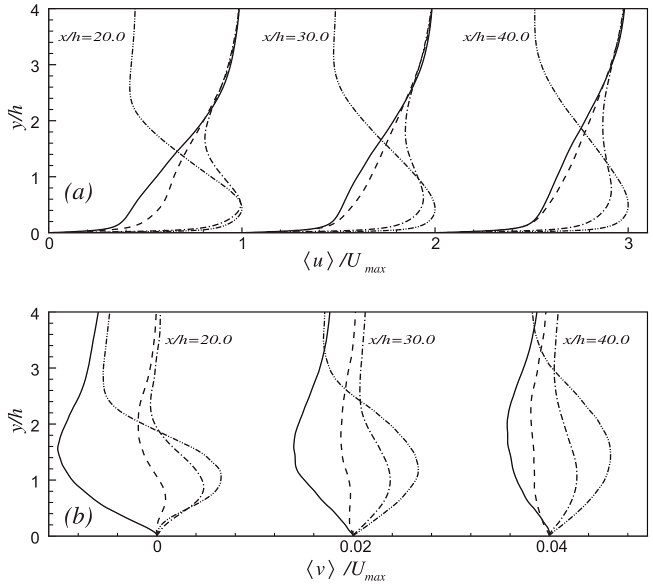

Fig. 11. (a) Mean streamwise velocity $\langle u\rangle/U_{max}$ and (b) mean wall normal velocity $\langle v\rangle/U_{max}$ profiles at streamwise locations $x/h = 20.0, 30.0$ and 40.0 for velocity ratios $M = 0.30$ (—), $M = 0.60$ (– – –), $M = 1.05$ (–·–) and $M = 2.30$ (–··–). The profiles are shifted by (a) $\langle u\rangle/U_{max} = 1.0$ and (b) $\langle v\rangle/U_{max} = 0.02$ for various streamwise locations.

followed by $M = 0.30, 0.60$ and 1.05, respectively. This behaviour follows from the fact that the shear layer strength and turbulence production depends on $|U_\infty - U_j|$ in the wake region. At $x = 20.0h$, $\langle u'u'\rangle/U_{max}^2$ has a complex transitional behaviour for $M = 0.60$ and 1.05. In the near wall region, jets with $M > 1.0$ have much higher $\langle u'u'\rangle/U_{max}^2$ values than $M < 1.0$. The near wall Reynolds stress production depends on jet velocity ratio M, or more appropriately on U_j, since U_∞ is fixed. The jets with $M > 1.0$ undergo rapid transition before $x = 20.0h$ (see Fig. 10(b)) and the near wall flow becomes fully turbulent. For $M < 1.0$ the near wall flow experiences a gradual transition (see Fig. 10(a)) and generates less turbulence at a distance of $x = 40.0h$. The wall normal Reynolds stress, $\langle v'v'\rangle/U_{max}^2$, has identical behaviour to that of $\langle u'u'\rangle/U_{max}^2$ in the wake region (see Fig. 12(b)).

Fig. 12(c) shows Reynolds shear stress ($\langle u'v'\rangle/U_{max}^2$) profiles with negative values near the wall. For $M > 1.0$ values, are higher than $M < 1.0$. This behaviour is identical to the near wall behaviour of $\langle u'u'\rangle/U_{max}^2$. On moving away from the wall, the shear stress changes sign, for $M > 1.0$, from negative to positive. The shear stress remains negative for $M < 1.0$. Similar to the normal Reynolds stresses, the magnitude of shear stress in the wake region is dependent on $|U_\infty - U_j|$. The positive and negative signs of $\langle u'v'\rangle/U_{max}^2$ for $M > 1.0$ and $M < 1.0$, respectively, are the result of different kinds of vortical structures in the wake.

Fig. 12 shows that for $M = 2.30$, the maximum values of Reynolds normal and shear stresses, in the outer shear layer region, are one fourth and one third that of the plane wall jet (Eriksson

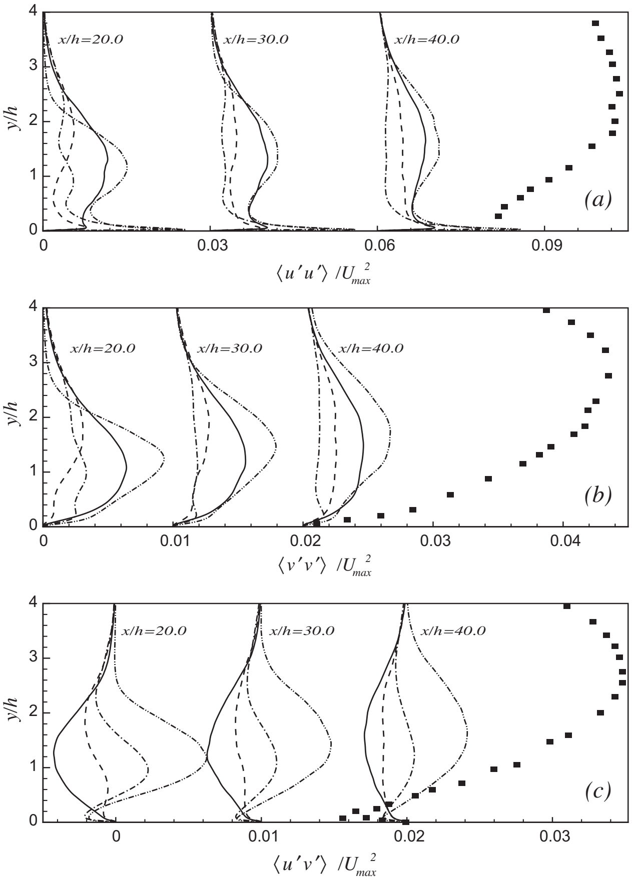

Fig. 12. Reynolds normal stresses (a) $\langle u'u'\rangle/U^2_{max}$, (b) $\langle v'v'\rangle/U^2_{max}$ and Reynolds shear stress (c) $\langle u'v'\rangle/U^2_{max}$ profiles at streamwise locations $x/h = 20.0, 30.0$ and 40.0 for velocity ratios $M = 0.30$ (—), $M = 0.60$ (– – –), $M = 1.05$ (–·–) and $M = 2.30$ (–··–). The profiles are shifted by (a) $\langle u'u'\rangle/U^2_{max} = 0.03$, (b) $\langle v'v'\rangle/U^2_{max} = 0.01$ and (c) $\langle u'v'\rangle/U^2_{max} = 0.01$ for various streamwise locations. (■) Eriksson et al. (1998) at $x/h = 40.0$.

et al., 1998), respectively. This results in a slower near wall transition and a reduced wall shear stress than that of a plane wall jet, as shown in Fig. 10(b).

4.4. Turbulent kinetic energy budgets

The turbulent kinetic energy (k) budget is given as;

$$\langle u_j\rangle \frac{\partial k}{\partial x_j} = \mathcal{P} + \mathcal{T} + \Pi + \mathcal{D} + \varepsilon, \tag{4}$$

where

$$\mathcal{P} = -\langle u'_i u'_j\rangle \frac{\partial \langle u_i\rangle}{\partial x_j}, \tag{5}$$

$$\mathcal{T} = -\frac{\partial}{\partial x_j}\left[\frac{1}{2}\langle u'_i u'_i u'_j\rangle + \langle u'_i \tau'_{ij}\rangle\right], \tag{6}$$

$$\Pi = -\frac{1}{\rho}\left\langle u'_i \frac{\partial p'}{\partial x_i}\right\rangle, \tag{7}$$

$$\mathcal{D} = 2\nu\nabla^2 k, \tag{8}$$

$$\varepsilon = -\nu\left\langle \frac{\partial u'_i}{\partial x_j}\frac{\partial u'_i}{\partial x_j}\right\rangle + \left\langle \frac{\partial u'_i}{\partial x_j}\tau'_{ij}\right\rangle, \tag{9}$$

are the production, turbulent transport, velocity pressure gradient, viscous diffusion and dissipation, respectively. The term on left hand side of the Eq. (4), is the mean flow advection of turbulent kinetic energy.

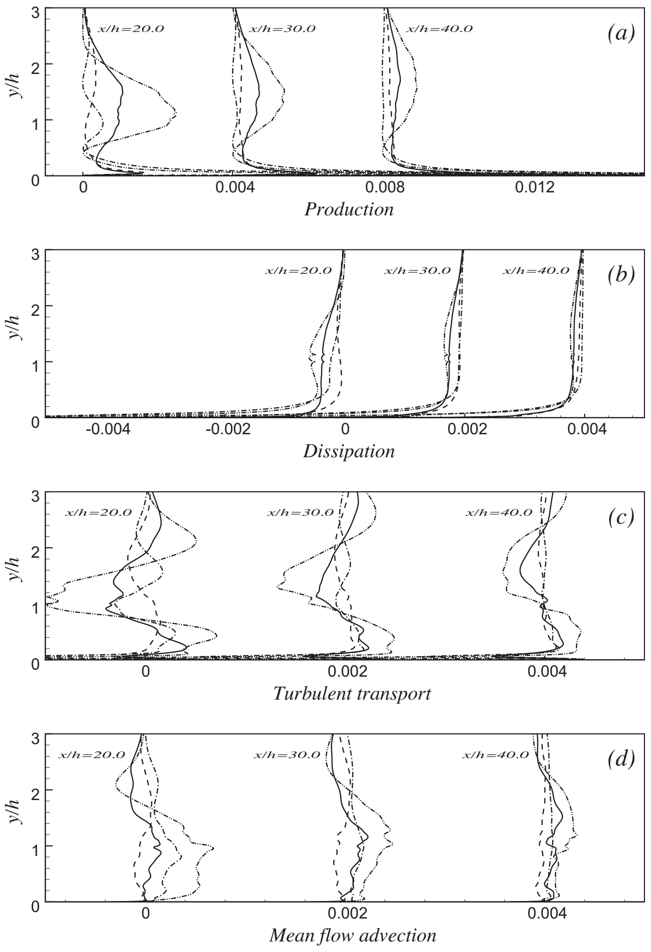

Fig. 13. Turbulent kinetic energy budgets (a) production, (b) dissipation, (c) turbulent transport and (d) mean flow advection profiles at streamwise locations $x/h = 20.0, 30.0$ and 40.0 for velocity ratios $M = 0.30$ (—), $M = 0.60$ (– – –), $M = 1.05$ (–·–) and $M = 2.30$ (–··–). The profiles are shifted by (a) production = 0.004, (b) dissipation = 0.002, (c) turbulent transport = 0.002 and (d) mean flow advection = 0.002 for various streamwise locations.

Fig. 13 shows the dominant terms of the budget, which are normalised by U^3_{max}/h. In the shear layer region the production has the highest values for $M = 2.30$ jet, followed by $M = 0.30, 0.60$ and 1.05 respectively. The near wall production increases with the increasing jet velocity. The production depends on the mean streamwise velocity gradient, which in the shear layer region depends on $|U_\infty - U_j|$. This explains the non-monotonic behaviour of the production with respect to increasing jet velocity ratio M. The non-monotonic behaviour of turbulence production also confirms the dependence of Reynolds stresses on $|U_\infty - U_j|$, as asserted in the previous section (see Fig. 12).

The production for jets with $M > 1.0$ goes to zero in the region ($y/h < 1.0$) where $U = U_{max}$. The dissipation in this region is balanced by turbulent transport from the wall and shear layer region. High negative turbulent transport is associated with high production in the shear layer region. This high negative turbulent transport region is located between two positive transport regions, one in the shear layer and the other near the wall. This behaviour has been observed in separated flows (Omidyeganeh and Piomelli, 2011; Silva Lopes et al., 2006).

The production of Reynolds normal stresses $\langle u'u'\rangle$, $\langle v'v'\rangle$ and shear stress $\langle u'v'\rangle$ are shown in Fig. 14. The production terms are normalised by U^3_{max}/h. The dominant terms in the Reynolds stress

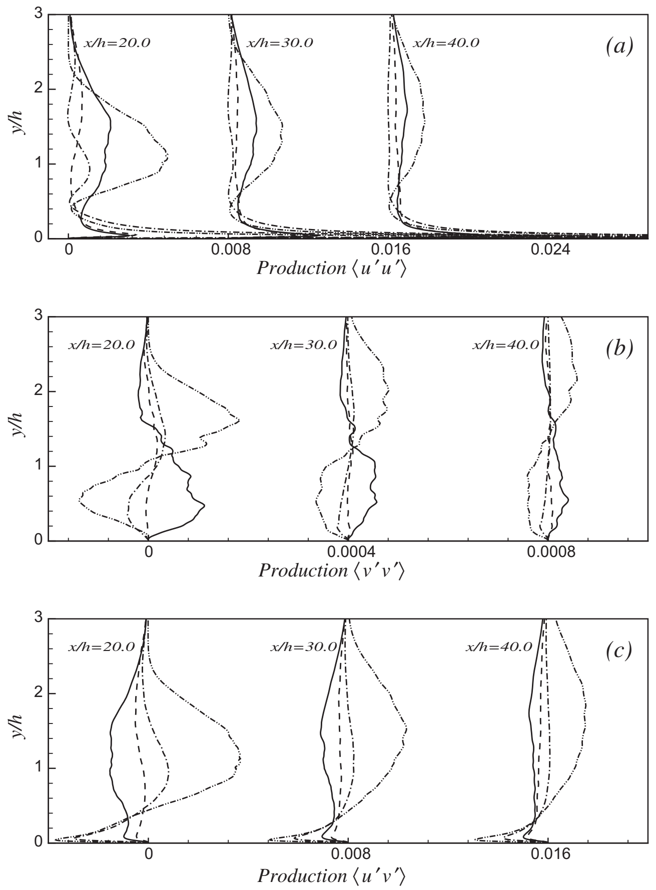

Fig. 14. Reynolds normal and shear stress production, (a) production of $\langle u'u'\rangle$, (b) production of $\langle v'v'\rangle$ and (c) production of $\langle u'v'\rangle$ profiles at streamwise locations $x/h = 20.0, 30.0$ and 40.0 for velocity ratios $M = 0.30$ (—), $M = 0.60$ (– – –), $M = 1.05$ (–·–) and $M = 2.30$ (–··–). The profiles are shifted by (a) production $\langle u'u'\rangle = 0.008$, (b) production $\langle v'v'\rangle = 0.0004$, and (c) production $\langle u'v'\rangle = 0.008$ for various streamwise locations.

production are $P_{\langle u'u'\rangle} \sim -2\langle u'v'\rangle\partial\langle u\rangle/\partial y$, $P_{\langle v'v'\rangle} \sim -2(\langle u'v'\rangle\partial\langle v\rangle/\partial x + \langle v'v'\rangle\partial\langle v\rangle/\partial y)$ and $P_{\langle u'v'\rangle} \sim -2(\langle u'v'\rangle\partial\langle v\rangle/\partial y + \langle v'v'\rangle\partial\langle u\rangle/\partial y)$ for $\langle u'u'\rangle$, $\langle v'v'\rangle$ and $\langle u'v'\rangle$ production, respectively. The production of $\langle u'u'\rangle$ is positive for all the values of M. The $\langle v'v'\rangle$ production term changes sign in the outer region. It is positive for $M = 2.30$ and becomes negative, whereas for $M = 0.30$ it is negative and becomes positive on moving towards the wall. In the outer region, the production of $\langle u'v'\rangle$ is negative for $M < 1.0$ and positive for $M > 1.0$. The production behaviour is determined by the dominant terms of production and the mean flow distribution given in Figs. 11 and 12. The Reynolds normal and shear stress production profiles also show a non-monotonic dependence on jet velocity ratio M in the outer region. This behaviour is similar to that of the turbulent kinetic energy production and has the same dependence on $|U_\infty - U_j|$ for $P_{\langle u'u'\rangle}$ and $P_{\langle u'v'\rangle}$.

4.5. Scaling behaviour of wall jet and boundary layer interaction

The scaling behaviour of plane wall jets is an important issue and has been discussed extensively, e.g. (Glauert, 1956; Bradshaw and Gee, 1962; Dejoan and Leschziner, 2005; George et al., 2000). For mean streamwise velocity profiles, inner scales for the near wall region and outer scales for outer shear layer give self-similar behaviour. In the presence of an external stream and wake these two scales are not sufficient to show self-similarity. The jet velocity ratio also determines the choice of velocity and length scale parameters to describe self-similarity. In this section different velocity and length scales will be used to determine the self-similar behaviour of wall jets with an external stream.

Fig. 15 shows the mean streamwise velocity and Reynolds stress profiles for various jet velocity ratios scaled with inner variables, i.e. shear velocity $\langle u_\tau\rangle$ and $\nu/\langle u_\tau\rangle$. Each jet velocity ratio has three profiles at locations $x = 20.0h, 30.0h$ and $40.0h$. The mean velocity plots also have log-law and $\langle u\rangle^+ = y^+$ curves. The inner variables give complete self-similarity only for near wall region. For $x = 30.0h$ and $M \geqslant 0.75$ mean velocity profiles have complete similarity up to $y^+ = 100.0$. Comparison with the log-law also shows that for $M \leqslant 0.75$, the mean flow recovers to a turbulent boundary layer by $x = 40.0h$. The scaling of Reynolds stresses u^+_{rms} and $\langle u'v'\rangle^+$ is also presented. Their behaviour is also identical to the mean streamwise velocity.

Fig. 16 shows scalings based on U_∞ and boundary layer thickness δ. The mean velocity profiles for jets with $M \leq 0.90$ show self-similar behaviour beyond $x = 30.0h$. The Reynolds stress profiles only partially collapse beyond $x = 30.0h$. This indicates incomplete scaling of the flow for the given domain length. For high velocity ratio jets $M > 0.90$, neither mean velocity nor Reynolds stress scale with boundary layer parameters up to $x = 40.0h$.

The plane wall jets show self-similar behaviour in the outer shear layer region when scaled with outer variables, i.e. U_{max} and $y_{1/2}$. As mentioned earlier, it is not possible to define $y_{1/2}$ for low velocity ratio jets. However, high velocity ratio jets resemble a wall jet and can be scaled with outer variables. Fig. 17 shows the mean velocity and streamwise Reynolds stress scaled profiles for high velocity ratio jets. The mean velocity profiles show similarity for $M \geqslant 1.35$. The profiles for $M = 2.30$ show similarity up to $y/y_{1/2} = 0.90$. The lower velocity ratio jets show similarity up to $y/y_{1/2} < 0.90$. The velocity profiles diverge in the wake and outer stream regions and the Reynolds stress profiles do not collapse completely. Only for $M = 2.30$, do the Reynolds stress collapse up to $y/y_{1/2} = 0.50$.

Zhou and Wygnanski (1993) have shown that wall jets with an external stream can also be scaled with $U_{max}, U_\infty, y_{1/2}$ and y_{max} (y location of U_{max}). They defined the velocity scaling as $(\langle u\rangle - U_\infty)/(U_{max} - U_\infty)$ and wall normal co-ordinates as $(y - y_{max})/(y_{1/2} - y_{max})$ and showed that this scaling works for $M > 2.0$. Nishino et al. (2010) have used a similar scaling for a Coanda jet. Fig. 18(a) shows mean velocity profiles with this scaling for higher velocity ratio jets. The profiles for $M = 2.30$ collapse beyond $x = 30.0h$. The lower velocity ratio jets show poor scaling with these parameters as compared to outer scales. For lower velocity ratio jets, the effects of an external stream are strong. The velocity scale defined by Zhou and Wygnanski (1993) seems suitable for low velocity ratio jets, however, the length scale is not. The effect of an external stream can be accounted for in the length scale if one uses a combination of boundary layer thickness δ with $y_{1/2}$. One of the possible y-axis scaling is given as $y/((\delta + y_{1/2})/2.0)$. Fig. 18*(b)* shows velocity profiles with $(\langle u\rangle - U_\infty)/(U_{max} - U_\infty)$ and $y/((\delta + y_{1/2})/2.0)$. The profiles for $M = 1.35$ and 1.50 give a better collapse than the original scaling of Zhou and Wygnanski (1993) (Fig. 18(a)).

4.6. Heat transfer characteristics

In the context of cutback trailing edge cooling, the most important heat transfer parameter is adiabatic film-cooling effectivenes $\eta_{aw} = (T_h - T_{aw})/(T_h - T_c)$. Here T_{aw} is the adiabatic temperature at the lower wall. The η_{aw} essentially gives a non-dimensional temperature distribution along the wall. This shows the effect of mixing of the external heated stream with the wall jet.

Fig. 19 shows the distribution of η_{aw} along the streamwise direction for various jet velocity ratios. The measurements of Kacker and Whitelaw (1969) for $M = 1.07$ are included for compar-

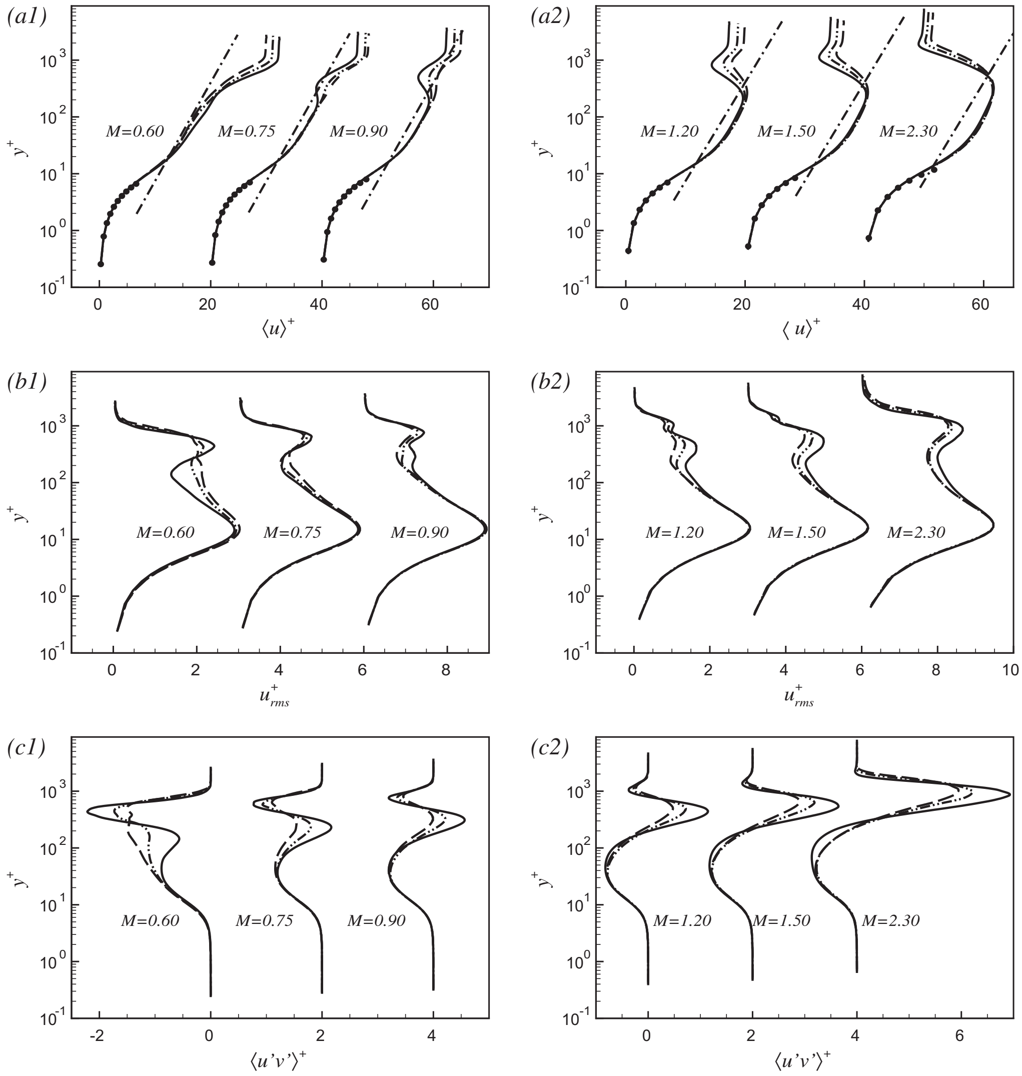

Fig. 15. Mean velocity and Reynolds stress profiles scaled with inner variables, where $M = U_j/U_\infty$. The profiles are given at $x = 20.0h$ (—), $30.0h$ (–···–) and $40.0h$ (– – –). Also shown $\langle u\rangle^+ = y^+$ (•) and log-law $2.5\log(y^+) + 5.0$ profile (–·–). The $\langle u\rangle^+$ profiles are shifted by $\langle u\rangle^+ = 20.0$, u^+_{rms} profile by $u^+_{rms} = 3.0$ and $\langle u'v'\rangle^+$ by $\langle u'v'\rangle^+ = 2.0$.

ison. The simulation predicted slightly higher values than the experiment for the closest velocity ratio jet of $M = 1.05$, however the trend is very similar. For the current simulations the effectiveness remains at unity at least up to $x = 6.0h$ for $M = 0.30$. This range extends to $x = 12.0h$ for $M = 2.30$. The effectiveness drops with streamwise direction and for $M = 0.30$ it reaches to 0.27 at $x = 40.0h$. However, with increasing jet velocity ratio the decay in effectiveness slows down substantially. The increase in velocity ratio up to $M = 0.60$ gives a large increase in effectiveness. This effectiveness increase slows down for higher M and the maximum effectiveness is achieved for $M = 1.05$. For $M > 1.0$, the streamwise decay in the effectiveness increases with increasing jet velocity ratio. However this decay is not as large as for jets with $M < 1.0$.

Fig. 20 shows the variation of η_{aw} with respect to increasing jet velocity ratio at two streamwise locations of $x = 25.0h$ and $40.0h$. The experimental results of Kacker and Whitelaw (1969) are also included for comparison. The comparison with measurements at both locations shows that the simulations appears to over predict the effectiveness. However, the effectiveness values in the experiment are not the direct temperature measurements at the wall. These values are measured as the concentration of a scalar species. This can give a lower value of the effectiveness. The figure shows that η_{aw} increases at a higher rate up to $M = 0.60$. Beyond this, η_{aw} increases at a lower rate attaining a maximum value at $M = 1.05$. For $M > 1.05$ there is a mild decay in the effectiveness. Schneider et al. (2012) presented an interesting behaviour for a wall jet flowing at an angle with the external stream and with a thicker wake plate ($t_w = 1.0h$). With this the effectiveness for an incoming highly turbulent wall jet increased for $M \in [0.35; 0.65]$. It then decreased for $M \in [0.65; 0.95]$ and finally increased again for $M \in [0.95; 1.40]$. In the current simulation for $M > 1.05$ effectiveness decreases with increasing M. However, the magnitude of the change in effectiveness and its rate of change with M are not as drastic as in Schneider et al. (2012).

The effectiveness is a manifestation of over all heat transport in the flow. To elucidate temperature transport Fig. 21 gives profiles of non dimensional mean temperature Θ, turbulent heat flux streamwise $\langle u'T'\rangle$ and the wall normal $\langle v'T'\rangle$ components and the mean wall normal convective heat flux $\langle v\rangle\langle T\rangle$. Note $\Theta = (T_h - \langle T\rangle)/(T_h - T_c)$ and the turbulent heat flux components are scaled with $U_{max}T_h$. In terms of non dimensional temperature, $\Theta = 0.0$ corresponds to the outer stream and $\Theta = 1.0$ to the incoming wall jet. Due to the mixing of the two streams, the near wall temperature $\Theta < 1.0$. The temperature profiles for $M = 0.30$ shows the strongest mixing and the smallest temperature gradients. For $M = 0.60$, the temperature gradient is higher than $M = 0.30$, which

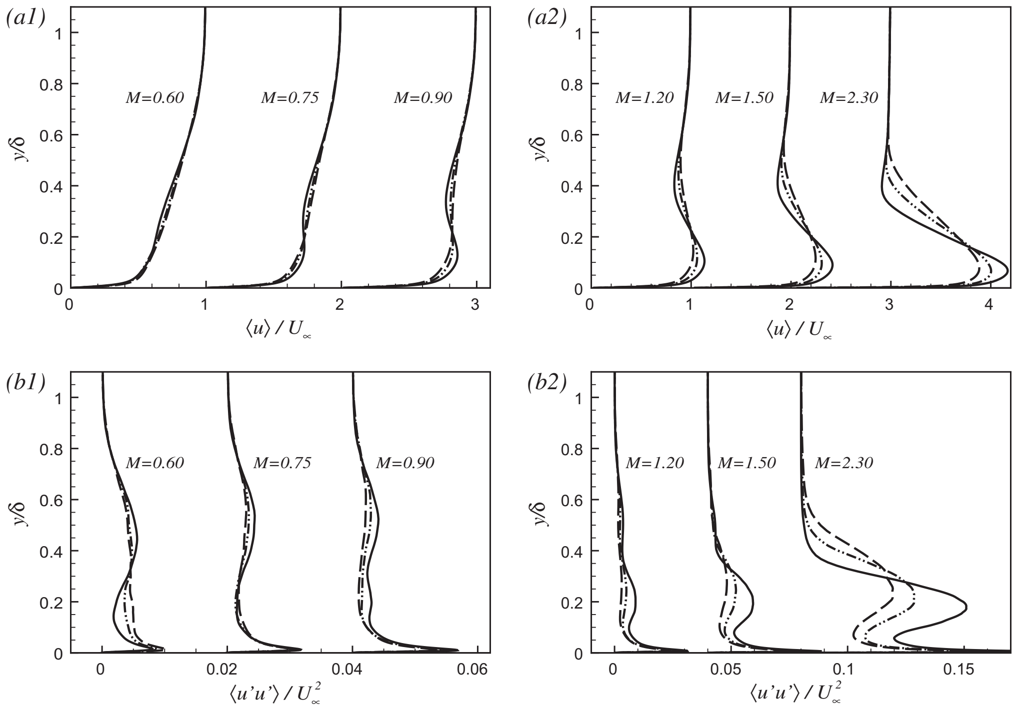

Fig. 16. Mean velocity and Reynolds stress profiles scaled with U_∞ and δ. The profiles are given at $x = 20.0h$ (—), $30.0h$ (–··–) and $40.0h$ (– – –). The profiles in (a1) and (a2) are shifted by $\langle u\rangle/U_\infty = 1.0$. The profiles in (b1) are shifted by $\langle u'u'\rangle/U_\infty^2 = 0.02$ and in (b2) by $\langle u'u'\rangle/U_\infty^2 = 0.04$.

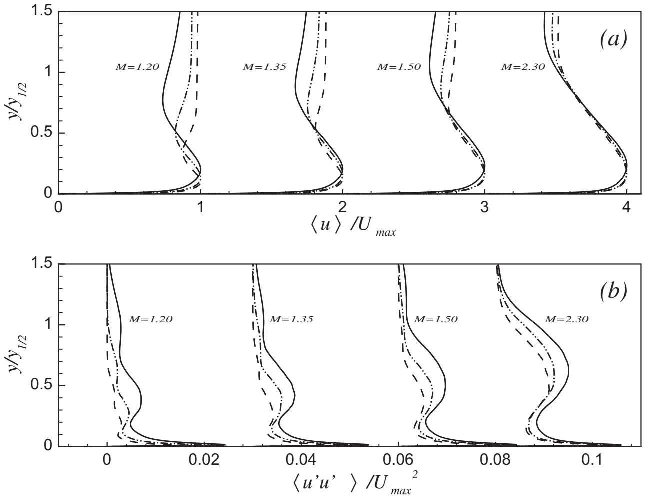

Fig. 17. Mean velocity and Reynolds stress profiles scaled with U_{max} and $y_{1/2}$. The profiles are given at $x = 20.0h$ (—), $30.0h$ (–··–) and $40.0h$ (– – –). The profiles in (a) are shifted by $\langle u\rangle/U_{max} = 1.0$. The profiles in (b) are shifted by $\langle u'u'\rangle/U_{max}^2 = 0.03$.

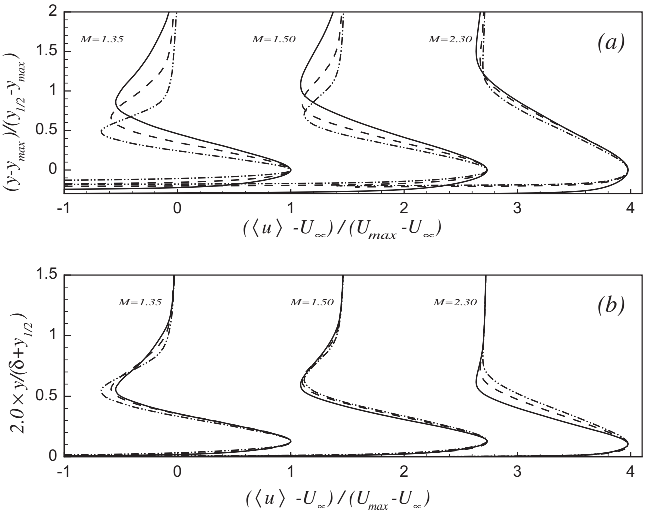

Fig. 18. Mean velocity profiles scaled with (a) $U_{max} - U_\infty, y_{max}$ and $y_{1/2}$ and (b) $U_{max} - U_\infty, \delta$ and $y_{1/2}$. The profiles are given at $x = 20.0h$ (—), $30.0h$ (–··–) and $40.0h$ (– – –). The profiles are shifted by $(\langle u\rangle - U_\infty)/(U_{max} - U_\infty) = 1.0$.

indicates slower mixing. For $M > 1.0$ this trend changes. The increasing jet velocity ratio increases mixing and the temperature gradient decreases. On moving in the streamwise direction, mixing increases and Θ along the wall decreases for all M.

The turbulent heat flux is a major component of heat transfer from the outer hot stream to the wall. The streamwise component $\langle u'T'\rangle/U_{max}T_h$ of turbulent heat flux (Fig. 21(b)) for jets with $M < 1.0$ is positive. This indicates heat transfer in the direction of the flow. Moreover, on moving downstream, the maximum level of $\langle u'T'\rangle/U_{max}T_h$ decreases for $M = 0.30$ and remains almost constant for $M = 0.60$. For higher velocity ratio jets with $M > 1.0$, $\langle u'T'\rangle/U_{max}T_h$ is negative, except for a region close to the wall where it changes sign and becomes positive. The negative values of $\langle u'T'\rangle/U_{max}T_h$ transport heat upstream. The wall normal flux component $\langle v'T'\rangle/U_{max}T_h$ (Fig. 21(c)) is negative for all the values of M. This negative flux is responsible for the transport of heat towards the wall. The magnitude of $\langle v'T'\rangle/U_{max}T_h$ increases with increasing jet velocity. There is a small decay in $\langle v'T'\rangle/U_{max}T_h$ on moving downstream. The trends shown by the turbulent flux components depend on the dominant term of their production. For the streamwise component, production is given as $P_{\langle u'T'\rangle} \sim -\langle u'v'\rangle\partial\langle T\rangle/\partial y$. This explains the positive and negative val-

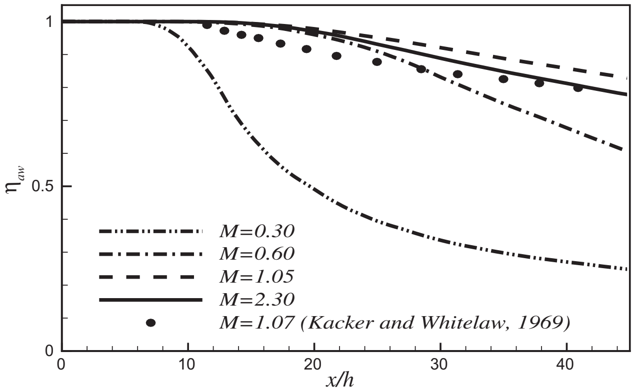

Fig. 19. Adiabatic film-cooling effectiveness for various velocity ratio jets.

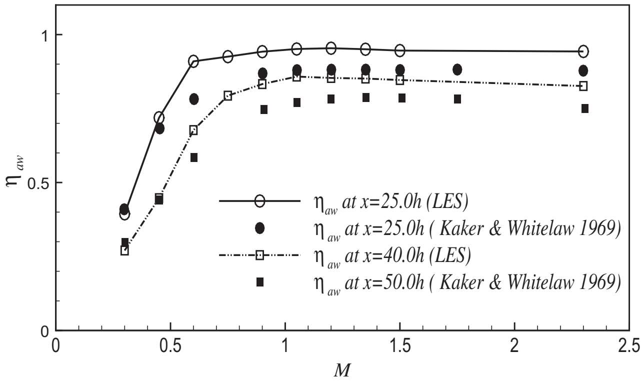

Fig. 20. Variation of adiabatic film-cooling effectiveness against velocity ratios at $x = 20.0h$ and $x = 40.0h$.

ues of $\langle u'T'\rangle/U_{max}T_h$ for jets with $M < 1.0$ and $M > 1.0$, respectively. They have exactly opposite signs from $\langle u'v'\rangle/U^2_{max}$ given in Fig. 12(c). The temperature gradient $\partial\langle T\rangle/\partial y$ is always positive for the given flow conditions. Also, at downstream locations $\langle u'T'\rangle/U_{max}T_h$ is higher for $M = 0.6$ than $M = 0.3$ because the temperature gradient is higher. The wall normal component production depends on $P_{\langle v'T'\rangle} \sim -\langle v'v'\rangle\partial\langle T\rangle/\partial y$. This results in negative values for $\langle v'T'\rangle/U_{max}T_h$, because $\langle v'v'\rangle$ is always positive (Fig. 12(b)).

Fig. 21(d) shows the profiles of mean convective wall normal heat flux $\langle v\rangle\langle T\rangle/U_{max}T_h$ for various values of M at different streamwise locations. The mean convective wall normal heat flux $\langle v\rangle\langle T\rangle$, is negative for jets with $M < 1.0$ and positive for $M > 1.0$. The negative values of $\langle v\rangle\langle T\rangle$ are responsible for the heat transfer from the outer stream to the wall. These values are also an order of magnitude larger than the corresponding turbulent heat flux, $\langle v'T'\rangle$.

Schneider et al. (2012) suggested that a large decay in effectiveness η_{aw} occurs when the turbulent heat flux is large and both of its components are negative. In the current situation, a large decay in η_{aw} occurs for $M = 0.30$, which has a low level of $\langle v'T'\rangle/U_{max}T_h$ and positive $\langle u'T'\rangle/U_{max}T_h$. The faster decay of effectiveness η_{aw} in the streamwise direction for $M < 1.0$ can be associated with the turbulent heat flux and the negative mean vertical velocity $\langle v\rangle$ or mean convective vertical flux $\langle v\rangle\langle T\rangle$, shown in Figs. 11(b) and 21(d), respectively. With a negative vertical velocity there is a dominant mean convection of the outer hot stream towards the wall. It mixes with the cold wall jet fluid and increases the near wall mean temperature. Increasing the jet velocity ratio reduces $\langle v\rangle$ and slows down the streamwise decay of η_{aw}. For $M > 1.0$ there is no mean convection towards the wall. In this case, only the turbulent heat flux is responsible for the mixing of the outer hot stream with the cold wall jet. The gradual reduction in η_{aw} for $M > 1.05$ shown in Fig. 20 is mainly due to the turbulent heat flux. With increasing M, both components of turbulent heat flux with negative signs have increasing magnitude as shown in Fig. 21. This results in greater mixing and an increase in the near wall temperature, i.e. a reduction in effectiveness.

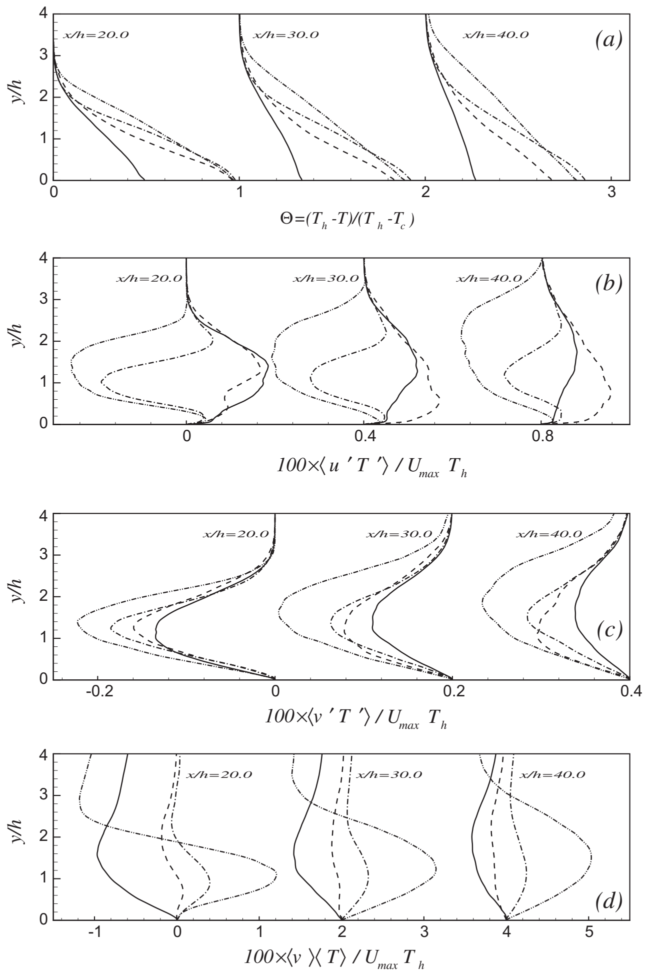

Fig. 21. (a) Non-dimensional temperature Θ, turbulent heat transfer, (b) streamwise $\langle u'T'\rangle/U_{max}T_h$, (c) wall normal $\langle v'T'\rangle/U_{max}T_h$ flux components and (d) mean convective wall normal $\langle v\rangle\langle T\rangle/U_{max}T_h$ flux profiles at streamwise locations $x/h = 20.0, 30.0$ and 40.0 for velocity ratios $M = 0.30$ (—), $M = 0.60$ (– – –), $M = 1.05$ (–·–) and $M = 2.30$ (–··–). The profiles are shifted by (a) $\Theta = 1.0$, (b) $\langle u'T'\rangle/U_{max}T_h = 0.4$, (c) $\langle v'T'\rangle/U_{max}T_h = 0.2$ and (d) $\langle v\rangle\langle T\rangle/U_{max}T_h = 2.0$ for various streamwise locations.

5. Conclusions

Highly resolved simulations of wall jets interacting with an external stream have been performed. The external stream is a fully developed turbulent boundary layer. It is separated from the wall jet by a thin wake plate. The jet velocity ratio M determines the development of the near and far field flow behaviour.

For the given range of jet velocity ratios $M = 0.30$—2.30, it is found that two different kinds of vortices form in the near wake region. The low velocity ratio jets with $M \leqslant 1.0$ give von-Karman type shed vortical structures in the wake region. These structures gradually mix the jet and external stream. With increasing jet velocity ratio alternate clockwise (CS) and counter-clockwise structures (CCS) disappear. For higher velocity ratio jets with $M > 1.0$ the JSL undergoes Kelvin–Helmholtz instability. As a result of this, a stream of counter-clockwise roll structures is formed. The roll structures interact with the external stream, and with each other and grow in size.

The large scale structures in the wake region determines the development of the mean flow field and subsequently heat transfer from the outer hot stream to the wall. In the current simulations, for $M < 1.0$ film-cooling effectiveness at any given streamwise location increases at a substantial rate with increasing jet velocity ratios. The maximum effectiveness is achieved at around $M = 1.05$. Further increases in jet velocity ratio for $M > 1.05$ results in a slow decay of the effectiveness. This defines two different ranges of M, where different mechanisms determine heat transport from the external hot stream to the wall. For $M < 1.0$, the CS induced negative mean vertical velocity $\langle v \rangle$ and negative turbulent heat flux component $\langle v'T' \rangle$ drive heat transfer. The mean flow convection of heat significantly outweighs heat transfer due to the turbulent heat flux. However, for $M > 1.0$ turbulent heat flux $\langle v'T' \rangle$, with a negative sign, is responsible for heat transfer towards the wall.

The variation of effectiveness with M in the current simulations shows the same trend as for thicker wake plates ($t_w \sim 1.0h$) given in Kacker and Whitelaw (1969) and Taslim et al. (1992). This is different from the variation of η_{aw} with respect to M given by Schneider et al. (2012). It suggests that the difference between the flow fields and the heat transfer trends between the current simulation and Schneider et al. (2012) is due to the angle of the wall jet flow with respect to the outer stream, a thicker wake plate, or the combination of both.

The scaling behaviour of the wall jet with the outer stream is also explored. It is found that the scaling parameters for the outer layer are highly dependent on M. Conversely, the inner layer is quite independent of M and scales well with inner variables, i.e. $\langle u_\tau \rangle$ and $\nu/\langle u_\tau \rangle$. It suggests that the near-wall Reynolds stresses and turbulence production have strong boundary layer characteristic. Moreover, in the far-field region, jets with $M < 1.0$ developed towards turbulent boundary layers. There is a strong interaction between the outer layer and the wall for the high velocity ratio jet ($M = 2.30$). This gives a reduced log-law for the mean streamwise velocity profile, similar to the wall jets. For $M > 1.0$ scaling parameters require further investigation.

Acknowledgements

A tremendous help from both the reviewers is greatly acknowledged for improving the original manuscript. Prof. Ugo Piomelli kindly provided the code used for the reported simulations. UK Turbulence Consortium provided computing time on HECTOR for these simulations.

References

Ahlman, D., Brethouwer, G., Johansson, A.V., 2007. Direct numerical simulation of a plane turbulent wall-jet including scalar mixing. Phys. Fluids 19, 065102.

Bradshaw, P., Gee, M.T., 1962. Turbulent wall jets with and without an external stream. British Aero. Res. Counc. R&M, 3252.

Dejoan, A., Leschziner, M.A., 2005. Large eddy simulation of a plane turbulent wall jet. Phys. Fluids 17, 025102.

Dubief, Y., Delcayre, F., 2000. On coherent vortex identification in turbulence. J. Turbul. 1, 1–22.

Dunham, J., 1968. The theory of circulation control by slot-blowing, applied to a circular cylinder. J. Fluid Mech. 33, 495–514.

Eriksson, J.G., Karlsson, R.I., Persson, J., 1998. An experimental study of a two-dimensional plane turbulent wall jet. Exp. Fluids 25, 50–60.

Glauert, M.B., 1956. The wall jet. J. Fluid Mech. 1, 625–643.

George, W.K., Abrahamsson, H., Eriksson, J., Karlsson, R.I., Lofdhal, L., Wosnik, M., 2000. A similarity theory for the turbulent plane wall jet without external stream. J. Fluid Mech. 425, 367–411.

Hunt, J.C.R., Wray, A.A., Moin, P., 1988. Eddies, streams, and convergence zones in turbulent flows. In: Proceedings of the 1988 Summer Program Studying Turbulence Using Numerical Simulation Databases, vol. 2. Stanford Universit, pp. 193–208.

Kacker, S.C., Whitelaw, J.H., 1969. The experimental investigation of the influence of slot-lip-thickness on the impervious-wall effectiveness of the uniform-density, two-dimensional wall jet. Int. J. Heat Mass Trans. 12, 1196–1201.

Kacker, S.C., Whitelaw, J.H., 1971. The turbulence characteristics of two-dimensional wall-jet and wall-wake flows. J. Appl. Mech. 38, 239–251.

Launder, B.E., Rodi, W., 1983. The turbulent wall jet measurements and modeling. Ann. Rev. Fluid Mech. 15, 429–459.

Leonard, B.P., 1979. A stable and accurate convective modelling procedure based on quadratic upstream interpolation. Comput. Meth. Appl. Mech. Eng. 19, 59–98.

Lin, W.E., Savory, E., 2010. Physical modelling of a downdraft outflow with a slot jet. Wind Struct. 28, 385–412.

Lund, T.S., Wu, X., Squires, K.D., 1998. Generation of inflow data for spatially-developing boundary layer simulations. J. Comput. Phys. 140, 233–258.

Martini, P., Schulz, A., 2004. Experimental and numerical investigation of trailing edge film cooling by circular coolant wall jets ejected from a slot with internal rib arrays. ASME J. Turbomach. 126, 229–236.

Meneveau, C., Lund, T.S., Cabot, W.H., 1996. A Lagrangian dynamic subgrid-scale model of turbulence. J. Fluid Mech. 319, 353–385.

Moin, P., Squires, K., Cabot, W., Lee, S., 1991. A dynamic subgrid-scale model for compressible turbulence and scalar transport. Phys. Fluids A 3 (11), 2746–2757.

Narashima, R., Narayan, K.Y., Parthasarathy, S.P., 1973. Parametric analysis of turbulent wall jets in still air. Aeronaut. J. 77, 355–359.

Nishino, T., Hahn, S., Shariff, K., 2010. Large-eddy simulations of a turbulent Coanda jet on a circulation control airfoil. Phys. Fluids 22, 125105.

Omidyeganeh, M., Piomelli, U., 2011. Large-eddy simulation of two-dimensional dunes in a steady, unidirectional flow. J. Turbul. 12 (42), 1–31.

Orlanski, I., 1976. A simple boundary condition for unbounded hyperbolic flows. J. Comput. Phys. 21, 251–269.

Patel, V.C., 1965. Calibration of the Preston tube and limitations on its use in pressure gradients. J. Fluid Mech. 23, 185–208.

Porté-Agel, F., Meneveau, C., Parlange, M.B., 2000. A scale-dependent dynamic model for large-eddy simulation: application to a neutral atmospheric boundary layer. J. Fluid Mech. 415, 261–284.

Radhakrishnan, S., Keating, A., Piomelli, U., Silva Lopes, A., 2006. Large-eddy simulations of high Reynolds-number flow over a contoured ramp. AIAA Paper 2006-899.

Radhakrishnan, S., Piomelli, U., Keating, A., 2008. Wall-modeled large-eddy simulations of flows with curvature and mild separation. ASME J. Fluids Eng. 130, 101203.

Schlatter, P., Orlu, R., Li, Q., Brethouwer, G., Fransson, J.H.M., Johansson, A.V., Alfredsson, P.H., Henningson, D.S., 2009. Turbulent boundary layers up to $Re_\theta = 2500$ studied through simulation and experiment. Phys. Fluids 21, 051702.

Schneider, H., von Terzi, D., Bauer, H.J., 2010. Large-eddy simulations of trailing-edge cutback film cooling at low blowing ratio. Int. J. Heat Fluid Flow 31, 767–775.

Schneider, H., von Terzi, D., Bauer, H.J., 2012. Turbulent heat transfer and large coherent structures in trailing-edge cutback film cooling. Flow Turbul. Combust. 88, 101–120.

Schneider, M.E., Goldstein, R.J., 1994. Laser doppler measurement of turbulence parameters in a two-dimensional plane wall jet. Phys. Fluids 6, 3116–3129.

Silva Lopes, A., Piomelli, U., Palma, J.M.L.M., 2006. Large-eddy simulation of a flow in an S-duct. J. Turbul. 7 (11), 1–24.

Spalart, P.R., 1988. Direct simulation of a turbulent boundary layer up to $R_\theta = 1410$. J. Fluid Mech. 187, 61–98.

Taslim, M.E., Spring, S.D., Mehlmann, B.P., 1992. An experimental investigation of film cooling effectiveness for slots of various exit geometries. J. Thermophys. Heat Transfer 6, 302–307.

Verhoff, A., 1963. The Two-Dimensional, Turbulent Wall Jet With and Without An External Free Stream. Princeton University and Office of Naval Research, Report No. 626.

Wygnanski, I., Katz, Y., Horev, E., 1992. On the applicability of various scaling laws to the turbulent wall jet. J. Fluid Mech. 234, 669–690.

Zhou, M.D., Wygnanski, I., 1993. Parameters governing the turbulent wall jet in an external stream. AIAA J. 31, 848–853.